# Atomic Ordering Enhanced Electrocatalytic Activity of Nanoalloys for Oxygen Reduction Reaction

Rameshwori Loukrakpam,[†] Shiyao Shan,[†] Valeri Petkov,[‡] Lefu Yang,[†] Jin Luo,[†] and Chuan-Jian Zhong*,[†]

[†]Department of Chemistry, State University of New York at Binghamton, Binghamton, New York 13902, United States
[‡]Department of Physics, Central Michigan University, Mt. Pleasant, Michigan 48859, United States

S *Supporting Information*

ABSTRACT: For oxygen reduction reaction (ORR) over alloy electrocatalysts, the understanding of how the atomic arrangement of the metal species in the nanocatalysts is responsible for the catalytic enhancement is challenging for achieving better design and tailoring of nanoalloy catalysts. This paper reports results of an investigation of the atomic structures and the electrocatalytic activities of ternary and binary nanoalloys, aiming at revealing a fundamental insight into the unique atomic-scale structure—electrocatalytic activity relationship. PtIrCo catalyst and its binary counterparts (PtCo and PtIr) are chosen as a model system for this study. The effect of thermochemical treatment temperature on the atomic-scale structure of the catalysts was examined as a useful probe to the structure—activity correlation. The structural characterization of the binary and ternary nanoalloy catalysts was performed by combining surface sensitive techniques such as XPS and 3D atomic ordering sensitive techniques such as high-energy X-ray diffraction (HE-XRD) coupled to atomic pair distribution function (PDF) analysis (HE-XRD/PDFs) and computer simulations. The results show that the thermal treatment temperature tunes the nanoalloy's atomic and chemical ordering in a different way depending on the chemical composition, leading to differences in the nanoalloy's mass and specific activities. A unique structural tunability of the atomic ordering in a platinum—iridium—cobalt nanoalloy has been revealed for enhancing greatly the electrocatalytic activity toward oxygen reduction reaction, which has significant implication for rational design and nanoengineering of advanced catalysts for electrochemical energy conversion and storage.
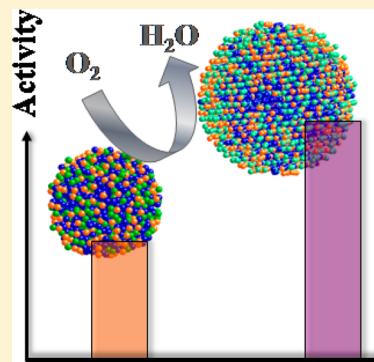
INTRODUCTION

In the search of platinum (Pt)-containing nanoalloy catalysts for oxygen reduction reaction (ORR),[1−12] one of the most important electrochemical processes in electrochemical energy conversion and storage,[1] strong evidence emerges that some ternary PtMM′ catalysts exhibit an unprecedented enhancement of the electrocatalytic activity over pure Pt and some of the best binary counterparts.[6−12] For example, ternary nanoalloys such as PtNiCo and PtVCo exhibit greatly enhanced mass and specific activities in comparison with Pt, PtNi, and PtCo for ORR in acidic electrolyte.[6,7,13,14] The observed enhancement may be related to a change in oxygen binding energies, but the atomic-scale structure may play a more important role. A key question, which has not been explored so far, is how the atomic ordering in ternary nanoalloys differs from that in their binary counterparts and correlates with the catalytic activity and stability. To answer it, we carried out a detailed structural study of terrnary nanoalloy PtMM′ catalysts, where M = Ir and M′ = Co, aimed at revealing the atomic ordering—catalytic property relationship. We concentrate on this ternary system for several reasons. First, binary nanoalloy catalysts (PtCo, PtNi, PtRu, etc.) have been extensively studied for ORR, and Pt_3Co_1/C has been shown to be the best among them.[15−17] Second, binary PtIr catalysts have been explored for methanol oxidation and oxygen evolution reactions[18] but not yet for ORR. Note that, in addition to its lower cost than Pt, Ir

is known to form a very strong alloy with Pt in the bulk phase which is resistant to acid corrosion. DFT calculations predict that the introduction of Ir to PtCo may result in an increased catalyst stability.[19] A recent kinetic study of IrCo binary catalyst indicated that the incorporation of Co to Ir could improve the catalytic activity and selectivity toward ORR.[20] Ir is also known to exhibit strong affinity for OH and O species, which may be exploited in the nanoalloy for producing a synergistic effect on the ORR, and in some cases an increased stability. Considering that Pt and Ir exhibit fcc-type structure in bulk while Co occurs in two phases—hexagonal (hcp) and face centered cubic (fcc)—alloying Co with fcc-type metals, i.e., Pt and Ir, is expected to stabilize the fcc-type structure. Therefore, the study of Ir in nanoalloys is of great interest in many fundamental areas, including the strong alloying effect and the increased stability of the alloy. Using surface sensitive techniques such as XPS and 3D atomic ordering sensitive high-energy X-ray diffraction (HE-XRD) coupled to atomic pair distribution function (PDF) analysis (HE-XRD/PDFs) and computer simulations, we determine the atomic-scale structures of the nanoalloy catalysts, providing important new insights into their correlation with catalytic properties.

■ EXPERIMENTAL SECTION

Chemicals. Platinum(II) acetylacetonate ($Pt(acac)_2$, 97%), iridium carbonyl ($Ir_4(CO)_{12}$, 98%), Co(II) acetylactonate ($Co(acac)_2$, 98%), 1,2-hexadecanediol (90%), octyl ether (99%), oleylamine (70%), and Nafion (5 wt %) were obtained from Aldrich. Octyl ether was from TCI (70%) and distilled for high purity, oleic acid (99%) was obtained from Alfa Aesar, and carbon black was from Ketjen. All the other solvents were of analytical grade and were used without further purification.

Synthesis of Nanoalloys. PtIrCo trimetallic nanoparticles were synthesized using a modified polyol method in octyl ether solvent.[9] In an organic media, Pt(II) acetylacetonate and cobalt(II) acetylacetonate were reduced with 1,2-hexadecanediol, and iridium carbonyl underwent thermal decomposition in the presence of oleic acid and oleylamine as capping agents at a temperature of 270 °C. For the synthesis of $Pt_{61}Ir_{24}Co_{15}$, 1.6877 g of 1,2-hexadecanediol, 0.5547 g of $Pt(acac)_2$, 0.2307 g of $Ir_4(CO)_{12}$, 0.6461 g of $Co(acac)_2$, 1.5 mL of oleylamine, and 1.5 mL of oleic acid were added to 180 mL of octyl ether solvent. The solution was purged with N_2, heated to 270 °C, and refluxed for 30 min. Then the solution mixture was cooled, and ethanol was added to precipitate out the brown nanopaticles, which were then resuspended in hexane. Similarly, PtIr and PtCo nanoparticles were synthesized using the same method in octyl ether solvent.[14] Details for the synthesis of $Pt_{45}Ir_{55}$ and $Pt_{52}Co_{48}$ are included in the Supporting Information.

Preparation of Electrocatalysts. The nanoparticles were supported on the carbon black. For the preparation of carbon-supported nanoparticles, a typical procedure involved suspending carbon black (Ketjen Black) in hexane, sonicating for ~3 h, and adding nanoparticles (in accordance with the required metal loading) into the suspension, sonication for another 1 h, followed by stirring for ~15 h. The resulted powder was collected and dried under N_2. The supported catalysts were further treated in a quartz tube furnace by first heating at 260 °C in N_2, or 10% O_2/90% N_2 for 30 min for removing the organic shells, and then calcined at 400 °C and 800 or 926 °C in 15% H_2/85% N_2 for 120 min. For the catalysts treated at the higher temperature, no significant differences in structure and activity were observed between 800 and 926 °C.

Instrumentation and Measurements. Thermogravimetric analysis (TGA), Transmission electron microscopy (TEM), high-resolution transmission electron microscopy–energy dispersive X-ray spectroscopy (HRTEM-EDS), inductively coupled plasma-optical emission spectroscopy (ICP-OES), X-ray photoelectron spectroscopy (XPS), X-ray powder diffraction (XRD), X-ray absorption fine structure (XAFS) spectroscopy, high-energy X-ray diffraction (HE-XRD) coupled to atomic pair distribution function (PDF) analysis, electroananlytical techniques, and fuel cell durability testings were used for the characterization of the nanoparticles and catalysts.

High-energy XRD measurements were performed at the beamline 11IDC, at the Advanced Photon Source, Argonne, using X-rays of energy 115 keV (λ = 0.1080 Å). The diffraction data were reduced to the so-called structure factors, $S(q)$, and then Fourier transformed to the corresponding atomic PDFs $G(r)$, using the relationship

$$G(r) = \frac{2}{\pi} \int_{q=0}^{q_{max}} q[S(q) - 1] \sin(qr) \, dq \tag{1}$$

where q_{max} = 25 Å^{-1} in the present experiments. The wave vector q is defined as $q = 4\pi \sin(\theta)/\lambda$, where θ is half of the scattering angle and λ is the wavelength of the X-rays used. Note, as derived, atomic PDFs $G(r)$ are experimental quantities that oscillate around zero and show positive peaks at real space distances, r, where the local atomic density $\rho(r)$ exceeds the average one ρ_0. This behavior can be expressed by the equation $G(r) = 4\pi r \rho_0[\rho(r)/\rho_0 - 1]$, which is the formal definition of the PDF $G(r)$. High-energy XRD and atomic PDFs have already proven to be very efficient in studying the atomic-scale structure of nanosized materials.[21]

In the crystalline lattices constrained modeling the experimental PDFs were approached with a model featuring a fcc-type structure that occurs in bulk noble and transition metals. In this type of modeling a PDF for an infinite fcc lattice is first computed. Then each of the coordination spheres of the perfect lattice is broadened by a convolution with a Gaussian function to take into account the presence of thermal (Debye–Waller type) and static local atomic displacements in NPs. At the same time the computed PDF is multiplied by a particle shape (spherical in our case) dependent function which is zero for distances longer than the size of the NPs being modeled. It is a simplistic approximation to the structure of real NPs but is useful since it allows (i) to verify the type of the atomic ordering and (ii) to obtain a set of structural parameters (e.g., lattice parameters) that may be used to distinguish between different NPs.

Reverse Monte Carlo (RMC) simulations featured atomic configurations with the size and shape (spherical) as determined by TEM and chemical composition as determined by ICP/XPS. The initial configurations were pieces of a perfect fcc-type lattices. In the simulations the position of each metal atom (Pt, Ir, and Co) from the model configurations was adjusted as to minimize the difference between the model and total experimental PDF. To increase the chemical specificity in the case of ternary nanoalloys Pt-differential PDFs obtained by complementary resonant high-energy XRD experiments were also used to guide the RMC simulations. During the simulations metal atoms were constrained (i) not to come closer than preselected distances equal to the sum of the respective atomic radii and (ii) to maintain as maximal (i.e., as close to 12) as possible coordination numbers, thus taking into account the close-packing nature of the fcc-type atomic ordering in nobel and transition metals. At the same time the energy of the configurations were optimized by minimizing pairwise (Lennard-Jones type) potentials taken from literature sources.

The catalysts were also characterized using a number of other techniques, including X-ray photoelectron spectroscopy (XPS), direct current plasma–atomic emission spectroscopy (DCP-AES), TGA analysis, TEM analysis, and Cu Kα powder XRD characterization (see Supporting Information for details).

Electrochemical measurements were performed using a microcomputer-controlled electrochemical analyzer (CHI600a, CH Instruments).The experiments were performed in three-electrode electrochemical cells at room temperature. All experiments were done with 0.1 M $HClO_4$ as electrolyte and was deaerated with high-purity nitrogen for cyclic voltammetry (CV) and then saturated with oxygen for rotating disk electrode (RDE) measurements. The potentials are given with respect to the reversible hydrogen electrode (RHE).
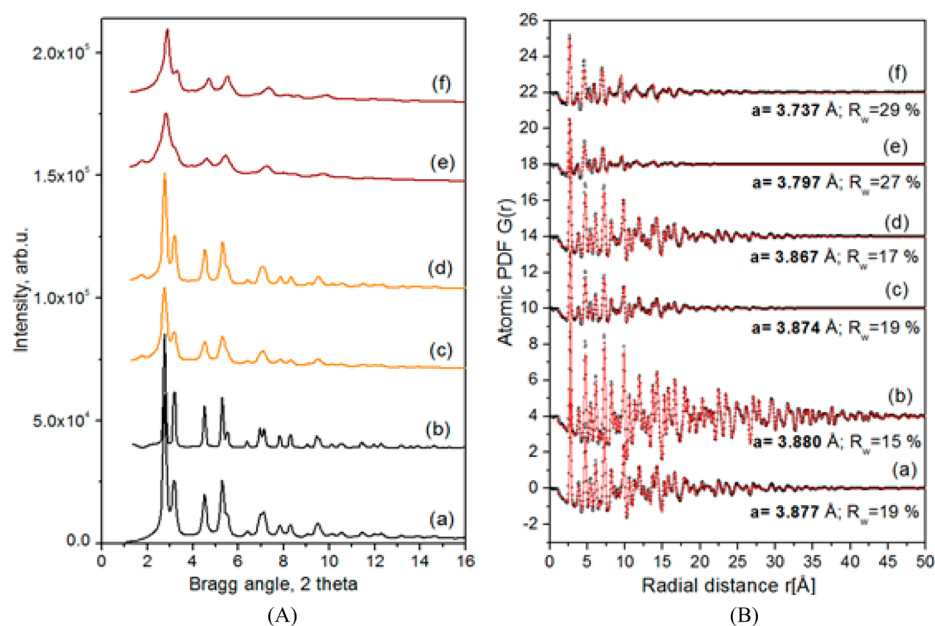
Figure 1. (A) HE-XRD ($\lambda = 0.1080$ Å) experimental patterns for $Pt_{45}Ir_{55}/C$ (a, b), $Pt_{73}Co_{27}/C$ (c, d), and $Pt_{25}Ir_{20}Co_{55}/C$ (e, f) treated at 400 (a, c, e) and 800 °C (b, d, f). (B) FCC-lattice constrained model fits (lines in red) to the experimental (symbols) atomic PDFs. The goodness-of-fit factors, R_w, and the refined fcc lattice parameters, a, are shown by each data set.

■ RESULTS AND DISCUSSION

Nanoalloy Structural Characteristics. Carbon supported PtIr, PtCo, and PtIrCo nanoparticles were thermochemically processed under two different temperatures: 400 and 800 °C. The compositions were determined by ICP-OES, whereas the average particle sizes were determined by TEM (Figure S1). Examples studied in this work include $Pt_{45}Ir_{55}/C$ (400 °C, 3.1 ± 0.6 nm; 800 °C, 4.7 ± 0.7 nm), $Pt_{73}Co_{27}/C$ (400 °C, 2.8 ± 0.4 nm; 800 °C, 3.2 ± 0.5 nm), and $Pt_{25}Ir_{20}Co_{55}/C$ (400 °C, 3.3 ± 0.6 nm; 800 °C, 4.9 ± 1.2 nm). There were small increases in particle sizes upon thermal processing at the higher temperature due to sintering. To compare the bulk metal composition obtained by ICP-OES with the relative surface metal composition and oxidation states, we did XPS analysis (Figure S2 and Table S1). We found that under the lower temperature treatment condition the surface composition of the binary nanoparticles was consistent with the bulk composition, whereas the ternary nanoparticles exhibited a relatively higher surface concentration of Pt at the expense of Ir and Co. Upon thermal treatment at 800 °C, a slight enrichment of Pt on the surface for the binary catalysts was observed. In contrast, a slight decrease of the relative surface composition of Pt was found for the ternary catalysts.

By comparing Pt 4f, Ir 4f, and Co 2p peaks for the catalysts treated at 400 and 800 °C (under H_2), subtle differences in the peak positions and shape were observed. The slightly asymmetric shapes and broadness of the peaks in the Pt 4f, Ir 4f, and Co 2p XPS spectra indicate the presence of higher oxidation states for some of the metal species in the nanoparticles. In terms of the binding energy (BE) values for Pt $4f_{7/2}$, Ir $4f_{7/2}$, and Co $2p_{3/2}$ peaks, slight shifts were observed for Pt 4f in both the binary and ternary catalysts with the temperature of treatment. In particular, $Pt_{73}Co_{27}/C$ and $Pt_{45}Ir_{55}/C$ showed a slight increase in the BE for Pt whereas a slight decrease was observed in $Pt_{25}Ir_{20}Co_{55}/C$. In general, these changes are very small, suggesting little change in the oxidation states of the metal species in the nanoalloys. The BEs

for Pt and Ir are consistent with those reported previously for nanoalloy catalysts of similar composition. The basic characteristics for Co 2p peak are also similar to those for other ternary catalysts.[7,14]

HE-XRD experiments coupled to PDF analysis[22] were carried out to reveal the nature of the atomic-scale structure in fine detail. A set of HE-XRD patterns for catalysts annealed at 400−800 °C is shown in Figure 1A. The peaks in the XRD pattern for PtIr/C are sharp indicating good crystallinity. The degree of crystallinity increases when the catalyst is treated at 800 °C. PtCo catalyst shows a lower degree of crystallinity, as compared to the case of PtIrCo. The crystallinity increases moderately at 800 °C. Peaks in the XRD pattern for PtIrCo catalyst processed at 400 °C are broad, indicating a great structural disorder. The catalyst remains structurally quite disordered even when processed at 800 °C.

Atomic PDFs extracted from the HE-XRD patterns for $Pt_{25}Ir_{20}Co_{55}/C$, $Pt_{73}Co_{27}/C$, and $Pt_{45}Ir_{55}/C$ thermally treated from 400 and 800 °C are shown in Figure 1B. At first the PDFs were approached with a model featuring a fcc-type structure that occurs in bulk noble and transition metals (see Supporting Information). As can be seen in Figure 1B, fcc-lattice model fits are of reasonable quality confirming the single phase state for the nanocatalysts. An inspection of the refined lattice parameters reveals the following pattern: for PtIrCo catalysts, a shrinking of the lattice parameter from 3.797 to 3.737 Å is observed with increasing the temperature of treatment. In the case of the bimetallic PtCo/C system, a shrinking of the lattice parameter is also observed from 3.874 Å at 400 °C to 3.867 Å at 800 °C. These results are in agreement with our previous findings.[7,9,14] A completely opposite trend is observed with PtIr/C. Here the fcc-lattice parameter increases from 3.877 to 3.880 Å with the temperature of treatment.

By closely examining the low-r part of the experimental atomic PDFs (Figure 2) the evolution of the first-neighbor metal−metal distances with changing the temperature of treatment can be discerned without any model assumptions.
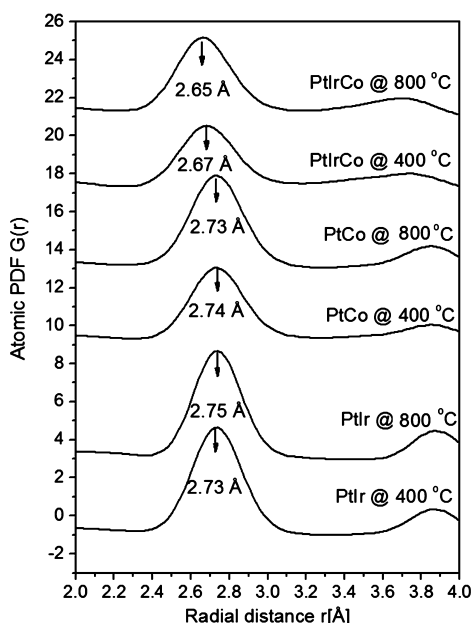
Figure 2. First peaks in the experimental atomic PDFs for $Pt_{25}Ir_{20}Co_{55}/C$, $Pt_{73}Co_{27}/C$, and $Pt_{45}Ir_{55}/C$ thermally treated at 400 and 800 °C. Positions of the peaks are estimated by Gaussian fits to the experimental data and are marked with arrows. Note the Pt–Pt bond distance in bulk Pt is about 2.76 Å and Co–Co bond distance in bulk Co is about 2.50 Å.

In the case of PtIrCo and PtCo the first-neighbor metal–metal distances shrink with increasing the temperature. By contrast, they increase in the case of PtIr. Also, the first neighbor metal–metal bond distances in the ternary catalyst are considerably shorter than those in the binary ones.

To reveal the atomic ordering in the studied nanoalloys in finer details, including exploring atomic and chemical ordering effects extending beyond a single unit cell of a periodic fcc-lattice, we performed reverse Monte Carlo (RMC) simulations (see Supporting Information). To increase the chemical specificity in the case of ternary nanoalloys Pt-differential PDFs obtained by complementary resonant high-energy XRD experiments were also used to guide the RMC simulations. Figure 3 shows representative snap shots of the atomic configurations resulted from the RMC simulations. Note (i) each configuration has the real stoichiometry and size of the nanoalloy being modeled and (ii) atomic PDFs computed from the configurations match the experimental PDF data very well (see Figure S3). Analysis of the model configurations shows that $Pt_{45}Ir_{55}$ catalyst (see Figure 3) is a random alloy of Pt and Ir when it is processed at 400 °C. When it is processed at 800 °C, PtIr catalyst tends to segregate into a structure with Ir core and Pt-enriched surface. This finding is qualitatively in agreement with the XPS-based analysis of the relative surface composition, which showed a 16% increase in Pt upon treatment at 800 °C (Table S1).

As shown in Figure 3 for $Pt_{73}Co_{27}$ catalyst processed at 400 °C, the RMC model features an alloy of Pt and Co where Co atoms show some preference to be closer to the center of the nanoparticles. For $Pt_{73}Co_{27}$ catalyst processed at 800 °C, the model features an alloy of Pt and Co with Co atoms being somewhat closer to surface of the particle. This redistribution is moderate in line with XPS analysis that gave $Pt_{73}Co_{27}$ and for $Pt_{52}Co_{48}$ (Table S1) surface composition for 400 and 800 °C processed catalysts, respectively.
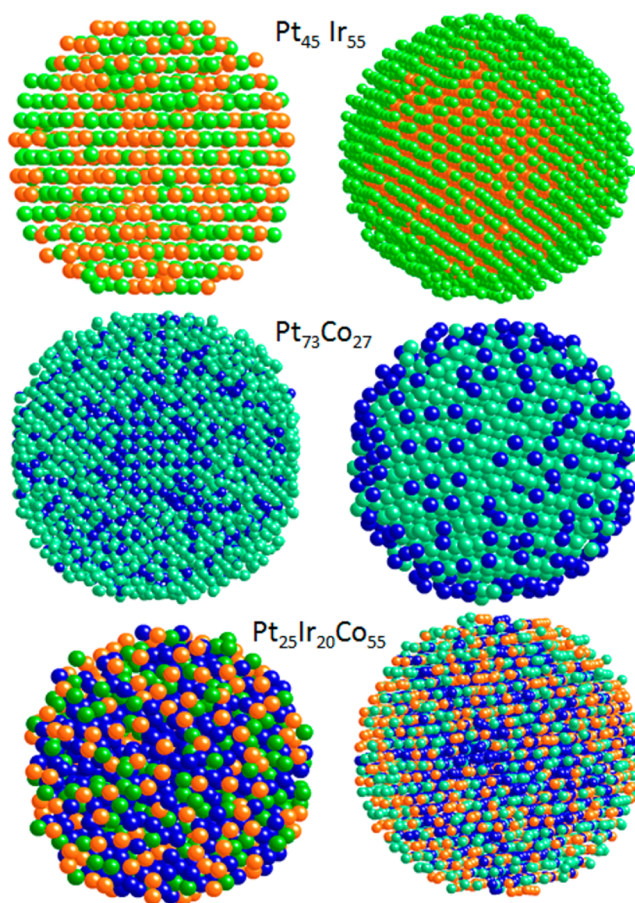

Figure 3. RMC constructed models for $Pt_{45}Ir_{55}$, $Pt_{73}Co_{27}$, and $Pt_{25}Ir_{20}Co_{55}$ processed at 400 °C (left panel) and 800 °C (right panel). (Pt atoms: green; Ir atoms: orange; Co atoms: blue). Note that the sizes of atoms are drawn not to scale to fit in the picture frame.

As shown in Figure 3 for $Pt_{25}Ir_{20}Co_{55}$ catalyst processed at 400 °C, the RMC model features an alloy where Co and Ir species tend to occupy the inner part of the nanoparticles while Pt atoms are present on the particle surface. Since XPS showed a somewhat smaller Pt composition than ICP-determined composition, the surface may have a smaller Pt composition than that in the bulk. In contrast, for $Pt_{25}Ir_{20}Co_{55}$ catalyst processed at 800 °C, the RMC model features a rather, but not completely, random type of alloy where Co, Pt, and Ir atoms are almost uniformly distributed across the nanoparticles. Based on XPS data, the surface seems to have a smaller Co composition than that in the bulk. The finding from the RMC modeling indicates that there are subtle changes of relative compositions across the nanoparticle for the ternary system as a function of temperature. The RMC modeling results reveal that the atomic species distribution across the nanoparticles depends strongly on (i) the binary/ternary composition and (ii) the thermochemical treatment temperature. A further confirmation of this RMC modeling derived dependence with the surface composition is needed since the changes derived from the XPS based analysis of the relative surface composition (only ~6% increase for $Pt_{25}Ir_{20}Co_{55}$ (Table S1)) are relatively small at this point of time.

The data for distributions of the bond angles as computed from the RMC generated atomic configurations (Figure 4A) show Co–Co–Co and Pt–Pt–Pt bond angles in view of the importance of Pt and Co metallic species in the catalytic
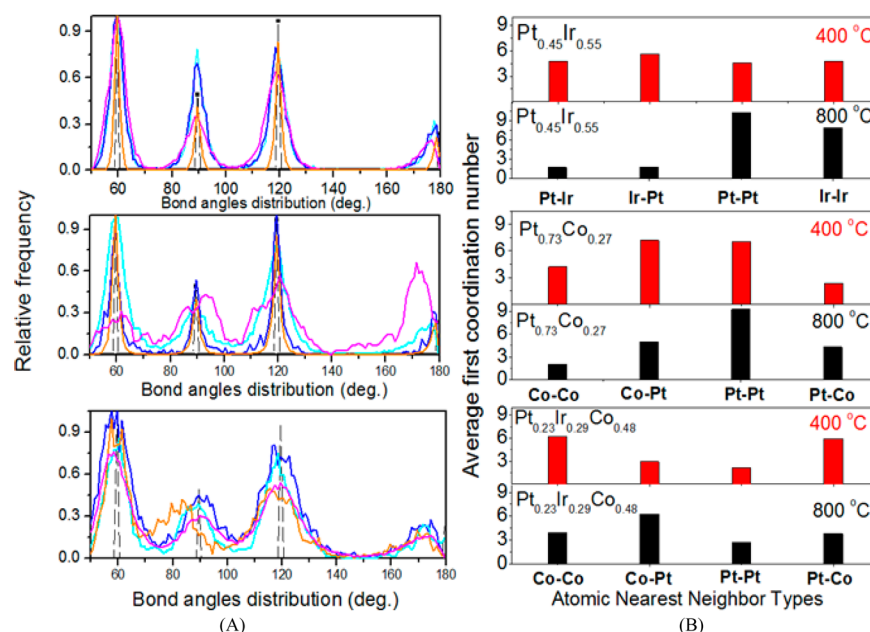
Figure 4. (A) Distribution of the bond angles in PtIr, PtCo, and PtIrCo processed at 400 and 800 °C. The bond angles occurring in a perfect fcc structure are given as vertical broken lines. The Pt−Pt−Pt and Ir−Ir−Ir bond angles for 4.7 nm $P_{45}Ir_{55}$, 3.2 nm $Pt_{73}Co_{27}$, and 4.9 nm $Pt_{23}Ir_{29}Co_{48}$ are given in brown and magenta lines, respectively. The Pt−Pt−Pt and Co−Co−Co bond angles in 3.1 nm $Pt_{45}Ir_{55}$, 2.8 nm $Pt_{73}Co_{27}$, and 3.3 nm $Pt_{23}Ir_{29}Co_{48}$ are given in cyan and blue lines, respectively. (B) Comparison of the first coordination numbers of selected atomic pairs in $Pt_{45}Ir_{55}/C$, $Pt_{73}Co_{27}/C$, and $Pt_{25}Ir_{20}Co_{55}$ processed at 400 and 800 °C as computed from the RMC model configurations shown in Figure 3.
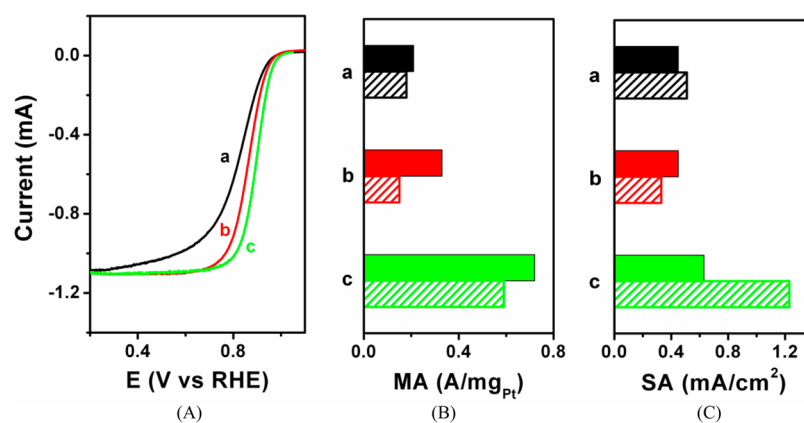
Figure 5. Electrocatalytic activities for ORR in O_2-saturated 0.1 M $HClO_4$: RDE curves for 400 °C treated catalysts (A) and mass (MA) (B) and specific activities (SA) (C) for 400 (filled bars) and 800 °C treated catalysts (patterned bars) (C). Catalysts: $Pt_{45}Ir_{55}/C$ (a), $Pt_{73}Co_{27}/C$ (b), and $Pt_{25}Ir_{20}Co_{55}/C$ (c).

reactions. All nanoalloys show features of face-centered-cubic packing since the respective bond angles cluster around the values of an ideal fcc structure. However, the broadening of the bond-angle distributions is different. As it can be expected, the broadening is smallest with PtIr nanoparticles that, per the respective experimental PDF data, show very good crystallinity. It increases with PtCo nanoparticles that show a moderate degree of crystallinity. The broadening of the bond-angle distribution, which reflects the degree of local structural disorder, is largest with ternary PtIrCo nanoparticles consistent with the very diffuse character of their XRD patterns (Figure 1).

The data for the first coordination numbers (CNs) of selected atomic pairs in PtIr, PtCo, and PtIrCo nanoalloy catalysts, computed from the respective RMC models (Figure 4B), show that the atomic species environment change with both composition and temperature of treatment. For PtIr, a

reduction of $CN_{(Pt-Ir)}$ and $CN_{(Ir-Pt)}$ ratio and a significant increase of $CN_{(Pt-Pt)}$ and $CN_{(Ir-Ir)}$ ratio are seen with increasing the processing temperature from 400 to 800 °C, consistent with a transition from a random alloy type to a Ir_core−Pt_shell type structure. For PtCo, the change in $CN_{(Co-Co)}/CN_{(Co-Pt)}$ ratio with processing temperature is less dramatic, consistent with a smaller degree of atomic rearrangement. For PtIrCo, the most significant change with the temperature is observed with $CN_{(Co-Co)}$ and $CN_{(Co-Pt)}$ ratio, consistent with a redistribution of Co species as demonstrated in Figure 3.

Nanoalloy Structure−Activity Correlation. Electrochemical active area (ECA) and electrocatalytic activity in terms of mass activity (MA) and specific activity (SA) for the catalysts were determined from measurements of voltammetric and RDE curves, respectively. Note that from a pure metal cost perspective normalizing the activity by combined Pt and Ir is perhaps a reasonable approach. However, we chose to

normalize it by Pt largely from fundamental perspective for the purpose of comparing with other Pt-based alloy nanoparticles. The ORR mass activity and specific activity are obtained from the kinetic current at 0.900 V in the RDE data (see Figure 5). Based on the analysis of the electrochemical data (Table S2), the MA of PtCo/C catalysts is found to decrease slightly with the increase in the treatment temperature. The ECA values showed some changes with treatment temperature, indicating a certain degree of sintering of the particles. Data for PtIr/C catalysts seem to follow a similar trend. In comparison with the two bimetallic catalysts, the trimetallic PtIrCo/C catalysts show a marked difference in the ECA data as well as in the current in the kinetic region. The ECA values are found to be very high as compared to PtCo system. The MA obtained for the ternary system is ∼2 times higher than that of the two bimetallic systems. A similar trend has been observed for another ternary catalysts, as for example PtNiCo/C when compared to PtCo/C and PtNi/C catalysts.[7,14]

On the basis of the results of the structure studies, it may be conjectured that the substantially shorter metal–metal distances in the ternary nanocatalysts (Figures 1B and 2) are responsible for their substantially improved catalytic properties. Also, the increase in SA from lower to higher temperature for the ternary nanoalloys is likely due to the further decrease in the metal–metal distances (Figures 1B and 2) and the changes in coordination numbers. In addition to a favorable change in Co–Pt first coordination number (see Figure 4B), there are also changes in Co–Ir, Pt–Ir, and Ir–Ir coordination numbers extracted from the RMC constructed model, which become 3, 3.6, and 3, respectively, all indicating an increased degree of alloying. As shown in Table 1, the thermal treatment changes

Table 1. Correlation between the ORR Electrocatalytic Activities and the Atomic PDFs Based Structure Data

catalyst	temp (°C)	1st M–M[a] (Å)	alloy characteristic	activity[b] MA	activity[b] SA
Pt₄₅Ir₅₅	400	2.73	random type	0.21	0.45
	800	2.75	Ir core with Pt-rich surface	0.18	0.51
Pt₇₃Co₂₇	400	2.74	Co-rich core	0.33	0.45
	800	2.73	slight Co enriched surface	0.15	0.33
Pt₂₅Ir₂₀Co₅₅	400	2.67	Co, Ir core, Pt-rich surface	0.72	0.63
	800	2.65	uniform distribution of Co, Pt, Ir	0.59	1.23

[a]Based on the position of first PDF peak. [b]MA (A/mg$_{Pt}$), SA (mA/cm^2).

the nanoalloy's atomic (e.g., first-neighbor distances) and chemical (e.g., first CNs) ordering. Moreover, the introduction of Ir in PtCo to form a ternary system was indeed shown to increase stability of the electrocatalytic activity.[9] In addition to the enhanced activity, the fact that the PtIrCo catalysts still showed a higher stability than PtCo indicates that the addition Ir played an important role in strengthening the stability.[9]

For PtIr, the structure change involves an evolution from a random type of alloy at 400 °C to an Ir_core-Pt_enriched surface structure at 800 °C. For PtCo, this change involves an evolution from a structure characterized with a Co-rich core at 400 °C to a structure with a slightly Co enriched in surface at 800 °C. In comparison, the ternary PtIrCo showed an evolution

from alloy with Co–Ir core and Pt-rich surface at 400 °C to an alloy where Co, Pt, and Ir species are more uniformly distributed across the nanoparticles at 800 °C.

For catalysts treated at 400 °C, both mass and specific activities are the highest for the ternary catalyst among the three catalysts studied here. The small decrease in mass activity upon increasing the temperature is due to a moderate increase in particle size. The specific activity for both PtIrCo and PtIr showed an increase whereas PtCo showed a small decrease with increasing the processing temperature. The increase of specific activity for the ternary nanoalloys is remarkable, by a factor of ∼2 in comparison with the relatively small increase for the binary PtIr, indicating the importance of adding a third chemical species to Pt-containing alloys. In correlation with the structural data, in particular the decrease in the first M–M distance and the formation of alloy featuring either an Co–Ir core with Pt-rich surface or a uniform distribution of Co, Pt, and Ir species across the entire nanoparticle, the ternary nanoparticles show a marked enhancement of the activity.

We note that it is very difficult to control the composition and size at the same time so that only the Ir's effect can be separated out; the catalysts studied in this work are still limited, which were largely based on a combination of several factors, including the fact that Pt₇₃Co₂₇ showed the best catalytic activity among different PtCo compositions. Therefore, the introduction of Ir into this binary system to form a ternary system would allow us to gain some fundamental understanding into the structural ordering or disordering properties. More compositions are yet to provide the confirmation studied along this line.

■ CONCLUSIONS

In conclusion, the results have revealed a clear difference between the atomic-scale structures of the ternary (PtIrCo) and the binary (PtCo and PtIr) nanoalloy catalysts. The difference is in terms of degree of structural disorder, near atomic neighbor distances, and first coordination numbers arising as a result of the particular chemical substitution and thermal treatment effects. In particular, mixing PtCo alloy with Ir, that virtually has the atomic size of Pt, results in a ternary catalyst that has substantially shrunk metal–metal distances. While our earlier work[9,14] showed that the ternary's lattice constant shrank more than the binary for low Co content (∼25%Co), we note that the difference of Co content in the PtCo and the ternary systems in this work does not allow us to directly compare the lattice shrinking, which requires a further investigation. Thermal treatment at higher temperatures results in a further shrinking in the metal–metal distances in the ternary nanoalloy while preserving its high degree of structural disorder. A redistribution of the metal species across the ternary nanoparticles is also observed. The atomic-scale structure differences between the binary and ternary nanoalloys are likely, at least in part, responsible for the higher electrocatalytic activity of PtIrCo/C in comparison with its binary counterparts. Obviously ternary nanoalloys offer extra structural tunability for improving the ORR catalytic activity. Harnessing this tunability for the design of even better catalysts is at the focus of our ongoing work. In view of the comparison between the ICP composition and the XPS composition being complicated by the presence of carbon support in the sample which may affect the depth profile of elements, and the ex-situ measurement which may not accurately reflect the true composition of the as-prepared samples due to air exposure and composition

evolution, an in-depth XPS study of the surface composition is also part of our further study.

ASSOCIATED CONTENT

Ⓢ Supporting Information

Addition experimental details, data, and author details for some of the references. This material is available free of charge via the Internet at http://pubs.acs.org.

AUTHOR INFORMATION

Corresponding Author
*Phone 1-607-777-4605; e-mail cjzhong@binghamton.edu (C.J.Z.).

Notes
The authors declare no competing financial interests.

ACKNOWLEDGMENTS

REFERENCES

(1) Zhong, C. J.; Luo, J.; Njoki, P. N.; Mott, D.; Wanjala, B.; Loukrakpam, R.; Lim, S.; Wang, L.; Fang, B.; Xu, Z. Fuel Cell Technology: Nano-Engineered Multimetallic Catalysts. *Energy Environ. Sci.* **2008**, *1*, 454−466.

(2) Wang, C.; Markovic, N. M.; Stamenkovic, V. R. Advanced Platinum Alloy Electrocatalysts for the Oxygen Reduction Reaction. *ACS Catal.* **2012**, *2*, 891−898.

(3) Gan, L.; Heggen, M.; O'Malley, R.; Theobald, B.; Strasser, P. Understanding and Controlling Nanoporosity Formation for Improving the Stability of Bimetallic Fuel Cell Catalysts. *Nano Lett.* **2013**, *13*, 1131−1138.

(4) Carlton, C. E.; Chen, S.; Ferreira, P. J.; Allard, L. F.; Shao-Horn, Y. Sub-Nanometer-Resolution Elemental Mapping of "Pt₃Co" Nanoparticle Catalyst Degradation in Proton-Exchange Membrane Fuel Cells. *J. Phys. Chem. Lett.* **2012**, *3*, 161−166.

(5) Yang, L.; Vukmirovic, M. B.; Su, D.; Sasaki, K.; Herron, J. A.; Mavrikakis, M.; Liao, S.; Adzic, R. R. Tuning the Catalytic Activity of Ru@Pt Core-Shell Nanoparticles for the Oxygen Reduction Reaction by Varying the Shell Thickness. *J. Phys. Chem. C* **2013**, *117*, 1748−1753.

(6) Wanjala, B. N.; Fang, B.; Petkov, V.; Zhu, P.; Loukrakpam, R.; Chen, Y.; Luo, J.; Yin, J.; Yang, L.; Shan, S.; et al. Design of Ternary Nanoalloy Catalysts: Effect of Nanoscale Alloying and Structural Perfection on Electrocatalytic Enhancement. *Chem. Mater.* **2012**, *24*, 4283−4293.

(7) Wanjala, B.; Fang, B.; Loukrakpam, R.; Chen, Y.; Engelhard, M.; Luo, J.; Yin, J.; Yang, L.; Shan, S.; Zhong, C. J. Role of Metal Coordination Structures in Enhancement of Electrocatalytic Activity of Ternary Nanoalloys for Oxygen Reduction Reaction. *ACS Catal.* **2012**, *2*, 795−806.

(8) Wanjala, B.; Fang, B.; Luo, J.; Chen, Y.; Yin, J.; Engelhard, M.; Loukrakpam, R.; Zhong, C. J. Correlation between Atomic Coordination Structure and Enhanced Electrocatalytic Activity for Trimetallic Alloy Catalysts. *J. Am. Chem. Soc.* **2011**, *133*, 12714−12727.

(9) Loukrakpam, R.; Wanjala, B. N.; Yin, J.; Fang, B.; Luo, J.; Shao, M.; Protsailo, L.; Kawamura, T.; Chen, Y.; Petkov, V.; et al. Structural and Electrocatalytic Properties of Nanoengineered PtIrCo Catalysts for Oxygen Reduction Reaction. *ACS Catal.* **2011**, *1*, 562−572.

(10) Chou, S. W.; Shyue, J. J.; Chien, C. H.; Chen, C. C.; Chen, Y. Y.; Chou, P. T. Surfactant-Directed Synthesis of Ternary Nanostructures: Nanocubes, Polyhedrons, Octahedrons, and Nanowires of PtNiFe: Their Shape-Dependent Oxygen Reduction Activity. *Chem. Mater.* **2012**, *24*, 2527−2533.

(11) Wang, C.; Li, D. G.; Chi, M. F.; Pearson, J.; Rankin, R. B.; Greeley, J.; Duan, Z. Y.; Wang, G. F.; van der Vliet, D.; More, K. L.; et al. Rational Development of Ternary Alloy Electrocatalysts. *J. Phys. Chem. Lett.* **2012**, *3*, 1668−1673.

(12) Wanjala, B.; Loukrakpam, R.; Luo, J.; Njoki, P. N.; Mott, D.; Shao, M.; Protsailo, L.; Kawamura, T.; Zhong, C. J. Thermal Treatment of PtNiCo Electroatalysts: Effects of Nanoscale Strain and Structure on Activity and Stability for Oxygen Reduction Reaction. *J. Phys. Chem. C* **2010**, *114*, 17580−17590.

(13) Yang, L.; Shan, S.; Loukrakpam, R.; Petkov, V.; Ren, Y.; Wanjala, B. N.; Engelhard, M. H.; Luo, J.; Yin, J.; Chen, Y.; et al. Role of Support-Nanoalloy Interactions in the Atomic-Scale Structural and Chemical Ordering for Tuning Catalytic Sites. *J. Am. Chem. Soc.* **2012**, *134*, 15048−15060.

(14) Loukrakpam, R.; Luo, J.; He, T.; Chen, Y.; Xu, Z.; Njoki, P. N.; Wanjala, B. N.; Fang, B.; Mott, D.; Yin, J.; et al. Nanoengineered PtCo and PtNi Catalysts for Oxygen Reduction Reaction: An Assessment of the Structural and Electrocatalytic Properties. *J. Phys. Chem. C* **2011**, *115*, 1682−1694.

(15) Stamenkovic, V. R.; Mun, B. S.; Arenz, M.; Mayrhofer, K. J. J.; Lucas, C. A.; Wang, G. F.; Ross, P. N.; Markovic, N. M. Trends in Electrocatalysis on Extended and Nanoscale Pt-Bimetallic Alloy Surfaces. *Nat. Mater.* **2007**, *6*, 241−247.

(16) Wang, C.; van der Vliet, D.; Chang, K.-C.; You, H.; Strmcnik, D.; Schlueter, J. A.; Markovic, N. M.; Stamenkovic, V. R. Monodisperse Pt₃Co Nanoparticles as a Catalyst for the Oxygen Reduction Reaction: Size-Dependent Activity. *J. Phys. Chem. C* **2009**, *113*, 19365−19368.

(17) Koh, S.; Toney, M. F.; Strasser, P. Activity-Stability Relationships of Ordered and Disordered Alloy Phases of Pt₃Co Electrocatalysts for the Oxygen Reduction Reaction (ORR). *Electrochim. Acta* **2007**, *52*, 2765−2774.

(18) Qiao, J.; Li, B.; Ma, J. Carbon-Supported IrM (M = V, Mn, Fe, Co, and Ni) Binary Alloys as Anode Catalysts for Polymer Electrolyte Fuel Cells. *J. Electrochem. Soc.* **2009**, *156*, B436−B440.

(19) Ma, Y.; Balbuena, P. B. Role of Iridium in Pt-based Alloy Catalysts for the ORR: Surface Adsorption and Stabilization Studies. *J. Electrochem. Soc.* **2010**, *157*, B959−B963.

(20) Yang, D.; Li, B.; Zhang, H.; Ma, J. Kinetics and Electrocatalytic Activity of IrCo/C Catalysts for Oxygen Reduction Reaction in PEMFC. *Int. J. Hydrogen Energy* **2012**, *37*, 2447−2454.

(21) Egami, T.; Billinge, S. J. L. *Underneath the Braggs' Peak*; Pergamon: Amsterdam, Netherlands, 2003.

(22) Petkov, V. 3D Structure of Nanosized Catalysts by High-Energy X-ray Diffraction. *Synchrotron Radiat. News* **2009**, *22*, 29−33.